Fine functional organization of auditory cortex revealed by Fourier optical imaging

Valery A. Kalatsky*†, Daniel B. Polley, Michael M. Merzenich*, Christoph E. Schreiner, and Michael P. Stryker

W. M. Keck Foundation Center for Integrative Neuroscience, Department of Physiology, University of California, San Francisco, CA 94143

Contributed by Michael M. Merzenich, July 11, 2005

We provide an overall view of the functional tonotopic organization of the auditory cortex in the rat. We apply a recently developed technique for acquiring intrinsic signal optical maps, Fourier imaging, in the rat auditory cortex. These highly detailed maps, derived in a several-minute-long recording procedure, delineate multiple auditory cortical areas and demonstrate their shapes, sizes, and tonotopic order. Beyond the primary auditory cortex, there are at least three distinct areas with fine-scale tonotopic organization, as well as at least one additional high-frequency field. The arrangement of all of these cortical areas is consistent across subjects. The accuracy of these optical maps was confirmed by microelectrode mapping in the same subjects. This imaging method allows fast mapping of the auditory cortex at high spatial resolution comparable to that provided by conventional microelectrode technique. Although spiking activity is largely responsible for the evoked intrinsic signals, certain features of the optical signal cannot be explained by spiking activity only, and should probably be attributed to other mechanisms inducing metabolic activity, such as subthreshold membrane phenomena.

optical imaging of intrinsic signals | rat | tonotopy | cortical maps

Mammalian auditory cortex consists of multiple functional fields. Multiple fields have been identified in a variety of species ranging from mice to primates, e.g., mouse (1), rat (2–4), cat (5–9), owl and macaque monkeys (10, 11), and human (12). The functional differences and significance of these cortical areas are largely unknown, and has been difficult to investigate without a reliable way of delineating cortical areal sizes and borders. The areas are thought to correspond to different auditory pathways and contribute toward distinct aspects of auditory information processing (13, 14). The number of fields in each species is itself controversial, ranging in the rat from estimates as low as two or three (15) to as many as five (2, 4).

Optical imaging of intrinsic signals, which measures changes in cortical light reflectance after local neural activation (16), has been used to great advantage in mapping functional representations in the visual (17–19), somatosensory (20–23), and olfactory (24–27) systems. By contrast, it has been difficult to generate high-resolution functional maps in the auditory cortex. The main contribution to the optical signal is due to the metabolically induced changes in the microcirculation (28) and, thus, inherits all cardiovascular artifacts. The major components of the hemodynamics are cyclic: heart beat, respiration, and vasomotor signal (29). Conventional methods of intrinsic optical imaging have been used for functional mapping of the auditory cortex (30–33). Here we demonstrate that a recently developed approach may allow generating functional maps of better quality by effectively removing cyclic artifacts from the continuously recorded signal.

We have recently proposed a general paradigm for stimulus presentation and analysis of optical imaging data: continuous-periodic stimulation combined with continuous data acquisition (34). Continuous stimulation offers the benefit of exhaustive coverage of stimulus space: every neuron is exposed to its optimal value of a stimulus parameter that is varied continuously. Periodic stimulation offers the advantage of effective separation of the stimulus-evoked responses from intrinsic noise by using Fourier analysis of the continuous data stream. This technique allows reconstruction of functional maps of much higher spatial resolution and lower noise than those obtained by conventional methods of optical imaging (30–33).

In this study, we report the functional division of the rat auditory cortex into at least five different fields revealed by high-resolution optical imaging of intrinsic signals and confirmed by electrophysiology. Compared to electrophysiology, imaging offers the advantage of a wide view of the cortical surface, thus simplifying the identification of several functional domains under the same conditions. These high-resolution maps can be obtained in <5 min, allowing detailed targeted electrophysiological and neuro-anatomical studies following the short noninvasive optical imaging session. Recently, we learned that similar imaging paradigm was used to map organization of ferret auditory cortex (35).

Materials and Methods

Acute procedures in all animals include a standard preparation for single-unit recording and optical imaging of intrinsic signal as described in refs. 34, 36, and 37. All experimental procedures were approved by the University of California, San Francisco, Committee on Animal Research.

Surgical Procedures. Sprague–Dawley rats (42 female, 6 male) were anesthetized with an i.p. injection of sodium pentobarbital (60–80 mg/kg). Atropine (0.1 mg/kg) and dexamethasone (0.5 mg per rat) were injected s.c. Rats were placed in a head-holder instrument, and the cisterna magnum was drained of cerebrospinal fluids to minimize edema and brain pulsation. A craniotomy was made over the area of interest (left temporal cortex usually, the right in two cases) and the dura mater reflected. Low-melting point agarose (3% in saline) and a glass coverslip were placed over the exposed area.

Imaging Procedures. High-resolution (4.6×4.6 mm^2 image area, 512×512 pixels at 7.5 frames per second rate after two by two spatial and four temporal binning) image streams of the cortical surface were stored after acquisition by a Dalsa 1M30 CCD camera controlled by custom software. The surface vascular pattern or intrinsic signal images were visualized with illumination wavelengths set by green (546 nm) or red (610 nm) interference filters, respectively. After acquisition of a surface image, the camera was focused 500–700 μm below the pial surface, and intrinsic signal images were acquired. A typical

A preliminary report of this work was presented in Kalatsky, V. A. & Stryker M. P. (2002) *Soc. Neurosci. Abstr.* 354.15 (abstr.).

Abbreviations: SPL, sound pressure level; CF, characteristic frequency; RF, receptive field; A1, primary auditory cortex; AAF, anterior auditory field; VAF, ventral auditory field; VAAF, ventral anterior auditory field; BF, best frequency.

*To whom correspondence may be addressed. E-mail: vkalatsky@uh.edu or merz@phy.ucsf.edu.

†Present address: Department of Electrical and Computer Engineering, University of Houston, 4800 Calhoun Road, Building 1, Room N308, Houston, TX 77204-4005.

imaging run lasted 10 min. Stimuli were delivered by a custom-made tube speaker inserted into the ear contralateral to the exposed cortex (right ear) or by a free-field speaker. The stimulus pattern was a sequence of tone pips ascending or descending exponentially in frequency and repeated with a period of 4–12 s (usually 6–8 s). The frequency range spanned three to four octaves, ranging from 1 to 40 kHz (usually 2–32 kHz). Onset-to-onset time for each map was a constant, ranging from 125 to 1,000 ms (usually 250 ms). Tone pip duration was 50 ms, with 5-ms rise and fall. Stimulus intensity was set to a constant value for each map between 20 and 70 dB sound pressure level (SPL).

Microelectrode Mapping Procedures. Microelectrode mapping was performed in a subset of rats after optical imaging ($n = 8$). The image of the surface vascular pattern acquired at the beginning of the imaging procedures was used to guide electrode placement. Tungsten microelectrodes (2 MΩ, FHC) were advanced 500–600 μm below the pial surface (layer 4/5). The evoked spikes from small clusters of neurons were collected at each site. Stimuli, pseudorandom tone pips from a grid of 45 frequencies over 3–5 octaves × 15 intensities over 0–100 dB SPL, centered at the characteristic frequency (CF), were delivered as described in *Imaging Procedures*.

Data Analysis. ***Optical imaging.*** Images were analyzed by using custom software. In short, a time series of light reflection values from each pixel was high-pass filtered by using a sliding window filter (the window was two cycles of the stimulus), and the fundamental Fourier component was extracted from the filtered series. The phases of the Fourier components were visualized as phase maps after cyclic color-coding. The amplitudes were plotted as strength of response gray-scale coded maps. See ref. 34 for more details. All maps shown here are presented at full resolution without spatial filtering. However, the optical best frequencies were obtained from low-pass filtered maps (circular kernel; diameter, 6 pixels or 50 μm) to reduce shot-noise induced high-frequency pixel-to-pixel fluctuations. RMS deviations of optical from electrophysiological maps were calculated by

$$\sqrt{\frac{1}{N}\sum_{i=1}^{N}\log_2(F_i^{op}/F_i^{el})^2},$$

where F_i^{op} and F_i^{el} are optically and electrophysiologically defined frequencies, respectively. Average cortical linear magnification factors were evaluated as $\log_2(F_i/F_j)/x_{ij}$, where F_i is optical frequency at site i and x_{ij} is cortical distance between points i and j. Magnification factors were calculated along directions perpendicular to iso-frequency lines. Optical noise level was calculated as strength of response in nonresponsive parts of the maps. ***Electrophysiology.*** Unit data analysis was similar to that described (4, 15, 36, 37). The spike counts were averaged over nearest neighbors. Besides conventional CFs, we also calculated four suprathreshold measures of receptive fields (RFs) at the stimulus intensities used for optical imaging; the lower and upper rows of spikes adjacent to the intensity of stimulation were averaged to reduce noise. (*i*) Best frequency: BF = $\sqrt{F_{lo} \times F_{up}}$, where F_{lo} and F_{up} are lower and upper frequencies that evoked responses at least 2 times higher than spontaneous activity. (*ii*) Center of mass of the spike distribution (BFCM):

$$\frac{\Sigma_i \log(F_i)\cdot N_i^{sp}}{\Sigma_i N_i^{sp}},$$

where F_i are pure-tone frequencies used for electrophysiology, N_i^{sp} is the number of spikes evoked by frequency F_i, and i enumerates all frequencies presented. (*iii*) Center of mass of the spike distribution restricted to the range of optical stimulation (BFCMR) was calculated with the same expression as BFCM, where i enumerates frequencies within the range of frequencies used for optical imaging, usually 2–32 kHz. (*iv*) Maximum of a cosine curve fitted into the profile of the spike distribution at the intensity and restricted to the range of stimulus frequencies used for optical imaging equivalent to fundamental Fourier component (Fourier). The last measure corresponds to the procedure followed to calculate optical BFs from the imaging data.

Results

Stimulus Pattern and Hemodynamic Delay. The main idea of the Fourier imaging is to present a temporally periodic stimulus and to analyze the component of the response at the stimulus frequency (34). The first challenge for using periodic-continuous imaging in the auditory modality was to design a stimulus that traverses the feature space in a continuous, periodic manner. Our solution is to impose periodicity by connecting the initial and final points of the stimulus parameter range, and thus to introduce a single discontinuity. The stimulus patterns used to assess tonotopy were staircases of tone pips, that is, ordered sequences of single pips with exponentially ascending or descending frequencies. Stepwise continuous stimuli were used to avoid habituation caused by slow FM sweeps. Typically, 16–32 tone pips were presented with 250- to 500-ms onset-to-onset time. In practice, distinguishing responses to the stimuli adjacent to the discontinuity did not present a dilemma because they are usually well segregated spatially on the cortical surface.

The next challenge is to account for the hemodynamic delay caused by the slow build-up of intrinsic signal after stimulation; one of our procedures for accomplishing it is the method of stimulus reversal (34). Reversal of the stimulus results in a reversal of the response sequence. However, the hemodynamic delay should be the same in both cases. Subtracting the response time to the reversed stimulus from the response time to the direct one produces an absolute response map that eliminates the delay (for more details, see *Stimulus Reversal Method for Delay Calculation* in *Supporting Text* and Fig. 5, which are published as supporting information on the PNAS web site).

Maps of absolute tonotopy can be computed by using two different strategies to overcome the hemodynamic delay. The first strategy is to measure the delay φ_d directly by restricting a test stimulus to a small region of stimulus space, playing a short part of the staircase (for more details, *see Validation of Mapping Procedures: Narrow-Band Stimulus Sequences* in *Supporting Text* and Fig. 6, which are published as supporting information on the PNAS web site). Because the association between the stimulus and the response is unambiguous in this case, the delay φ_d can be obtained by subtracting the response time from the stimulation time. Knowing this delay one can then shift the whole map by $-\varphi_d$ back to its absolute position. Second, the delay can be estimated from reference microelectrode recordings (see Fig. 2).

Multiple Auditory Fields: Comparison with Electrophysiology. Absolute tonotopy maps of the rat auditory cortex corrected by the method of the stimulus reversal are shown in Fig. 1*a*. Four distinct areas are clearly visible in the map: dorsal auditory field or primary auditory cortex (A1), anterior auditory field (AAF), ventral auditory field (VAF), and ventral anterior auditory field (VAAF). The borders of these tonotopic areas (Fig. 1*c*) were identified as follows: (*i*) the cortical regions responsive to the central part of the stimulus range were outlined. These regions appear as yellow in Fig. 1*c* and correspond to the cortical representation of 8 kHz, which was the center of the stimulation range measured in log-scale (2–32 kHz). (*ii*) These central islands were inflated perpendicular to the iso-frequency lines, both in the direction of high and low frequencies, until either the

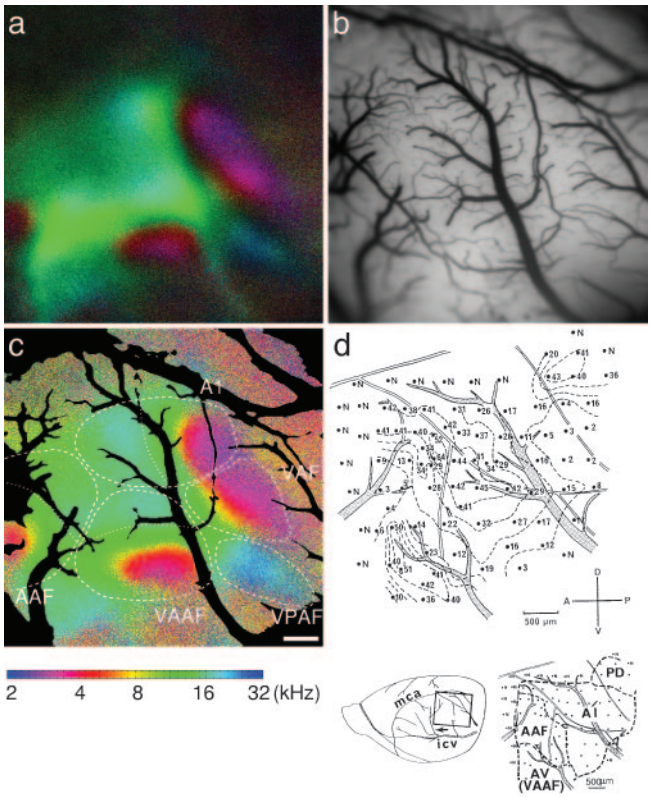

Fig. 1. Maps of multiple topographic areas in rat auditory cortex. (*a*) Polar map (hue encodes response phase and lightness encodes response magnitude) of absolute tonotopy. The hemodynamic delay was removed by the method of the stimulus reversal. (*b*) Surface vessel pattern from the same animal. (*c*) The same map as in *a* plotted as a phase map with overlaid vessel pattern from *b*. The contours outline identified auditory fields. The dotted lines, drawn at ≈16 kHz, outline the high-frequency region. The large uniform region (appearing as green) has a fine spectral structure that is emphasized on the map of double phase (Fig. 5*g*). (*d*) Frequency representation of the rat auditory cortex constructed by using standard electrophysiological mapping technique. A, anterior; D, dorsal; P, posterior; V, ventral; VPAF, ventral posterior auditory field. (Scale bar, 500 μm.) [Image in *d* reproduced with permission from ref. 2 (Copyright 1988, The Japan Academy, Tokyo).]

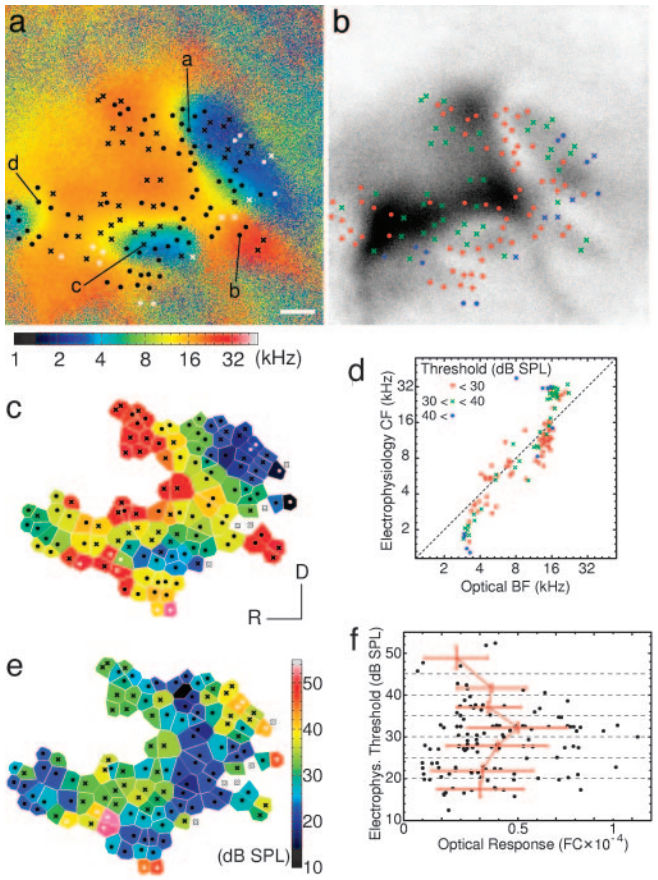

Fig. 2. Maps of multiple tonotopic areas in rat auditory cortex and comparison with electrophysiology in the same subject. (*a*) Optical phase map of tonotopy, noncyclically color coded (same subject as in Figs. 1 and 5). Symbols mark sites of microelectrode recordings: white crosses, no response; white circles, CF >40 dB SPL (intensity of stimulation for optical imaging); black crosses, CF >30 dB and <40 dB SPL; black circles, CF <30 dB SPL. Tuning curves from sites labeled as a, b, c, and d are shown in Fig. 3. (*b*) Map of optical response amplitude. (*c*) Map of CFs obtained by standard electrophysiological techniques (125 multiunit sites) in the same subject. (*d*) Correlation between optical imaging BFs and electrophysiological CFs. $n = 120$ (five sites elicited no response), slope, 1.30; intercept, −1.00 octave; $R^2 = 0.91$; RMS deviation = 0.60 octave; CF below 40 dB SPL: $n = 110$; slope, 1.26; intercept, −0.88 octave; $R^2 = 0.93$; RMS, 0.52 octave; CF below 30 dB SPL: $n = 67$; slope, 1.06; intercept, −0.31octave; $R^2 = 0.89$; RMS, 0.46 octave. Note that central regions of A1, AAF, and VAAF (as outlined in Fig. 1*c*) appear as islands surrounded by regions of weaker response. (*e*) Map of CF thresholds obtained by standard electrophysiological techniques. (*f*) Correlation between amplitude of optical response and electrophysiological CF thresholds. To calculate the average response, shown in red, the range of thresholds was divided by horizontal dashed lines (5-dB spacing), and both optical response and electrophysiological threshold for points inside these domains were averaged. The amplitude of optical response is a nonmonotonic function of electrophysiological CF thresholds. FC, fractional change; R, rostral; D, dorsal. (Scale bar, 500 μm.)

boundary reached the areas where optical response dropped down to the noise level (usually low frequencies) or the boundaries of different areas collided (usually high frequencies). (*iii*) The cortical space between the areas that appear as mirror pairs (e.g., VAF and VAAF) was approximately equally distributed. (*iv*) The inflation toward the high frequencies, beyond 16 kHz (the 16-kHz boundaries are shown as dotted lines in Fig. 1*c*), was somewhat arbitrary because distribution of the cortical space representing frequencies >16 kHz among A1, VAF, VAAF, and AAF was not obvious.

We identified a ventral posterior auditory field in the majority of rats. The high-frequency divisions of areas A1, AAF, VAF, and VAAF coalesce in the dorsal-anterior part of auditory cortex. It can be difficult to identify AAF in some subjects, as it is often occluded by an ascending branch of the inferior cerebral vein (ICV, Fig. 1*d*). Area VAAF is a mirror image of areas VAF, and possibly of AAF. Areas A1 and VAF appear as continuations of each other that may appear as one extended field. The extended A1-VAF area was divided into two fields for the following reasons. (*i*) A1 has a well pronounced posterior–anterior tonotopic axis, where the low frequencies are represented at the posterior end and the high at the anterior one (15), whereas the VAF's tonotopic axis is tilted by ≈45° relative to that of A1. (*ii*) Area A1 tonotopic axis extends to 32 kHz and higher at the anterior extremity, whereas the representation of high frequencies in the area VAF is mostly restricted to 16 kHz because it is limited in its anterior–dorsal extension by the tonotopic gradient of area VAAF, which runs in the opposite direction. (*iii*) There is a strong compression of optical phase response (Figs. 1*c* and 5 *c* and *d*) as well as a drop of response amplitude (Figs. 1*a* and 5 *e* and *f*) between these two areas. (*iv*) Finally, there have been studies (e.g., ref. 38) reporting that the temporal properties of neurons located in an approximately similar region are different from those of neurons located in A1.

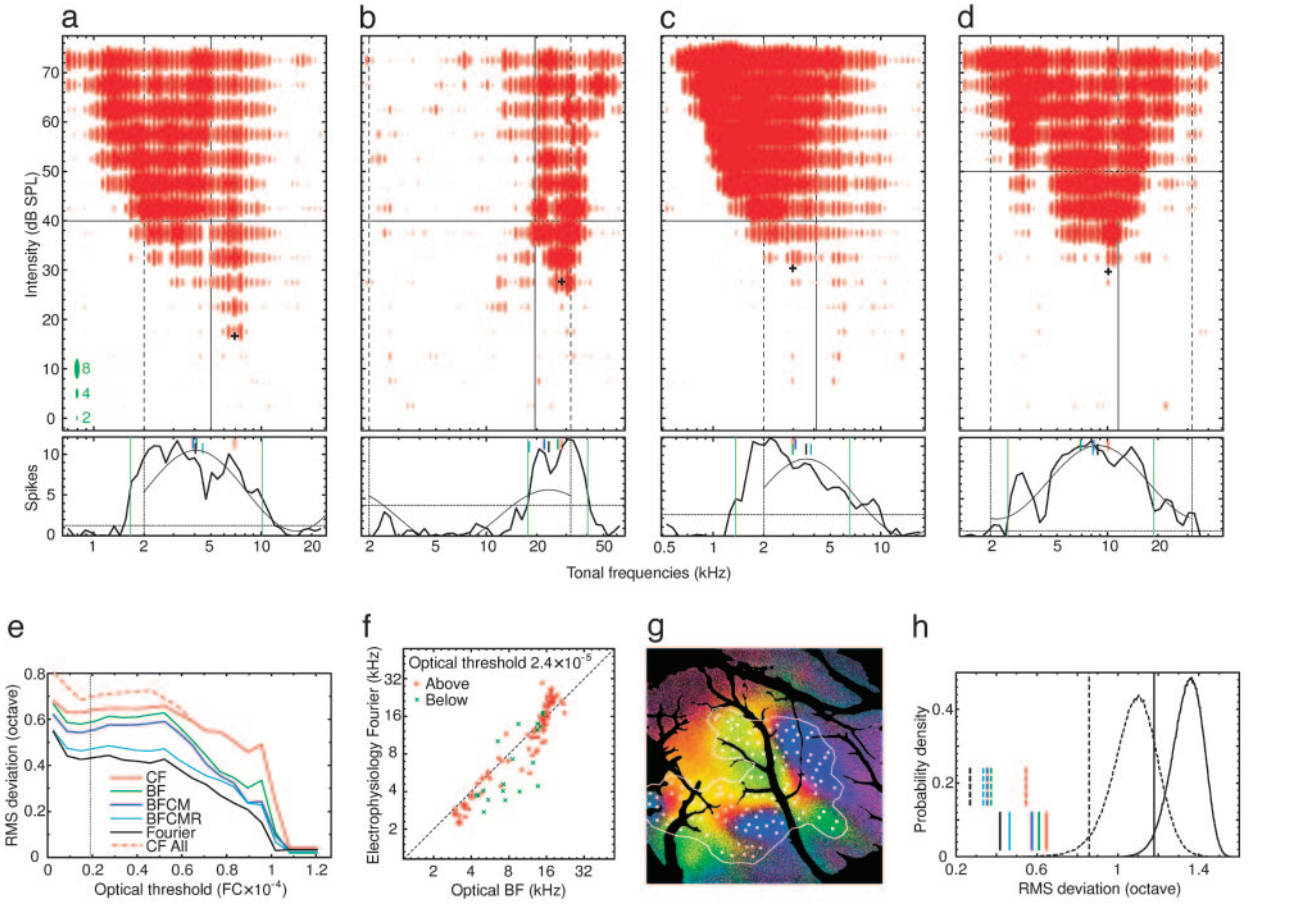

Fig. 3. Comparison of optical BFs and electrophysiological measures. (*a–d*) (*Upper*) Tuning curves acquired at the sites marked as a, b, c, and d in Fig. 2*a*. The black cross labels CF. Horizontal line, intensity of stimulation for optical imaging; vertical solid line, optical BF; legend (shown in green), correspondence between sizes of ellipses and number of spikes. (*Lower*) Profiles of spike distributions at the intensity of stimulation. The cosine curve is the fundamental Fourier component fitted into the spike distribution between 2 and 32 kHz. The five short vertical lines mark the measures of RFs, same color code as in *e*. Long green vertical lines show lower (F_{lo}) and upper (F_{up}) frequencies used to define BF. Horizontal line, level of spontaneous activity. (*e*) RMS deviation of the optical BFs from the electrophysiological measures as a function of optical response threshold and optical BFs from ascending staircase map. Solid red curve, CFs with threshold below stimulation for optical imaging (40 dB SPL, $n = 110$); dashed red curve, all CFs ($n = 120$). Vertical dashed line, optical noise level. (*f*) Correlation between optical BFs from averaged map and electrophysiological Fourier frequencies. (*g*) Ascending phase map with overlaid vessel pattern used for random penetration simulations. (*h*) Probability density of RMS deviation of random penetrations for two values of optical response threshold: 30% (solid lines) and 60% (dashed lines). Long vertical lines, lower 95% confidence interval; short lines, RMS deviation for five electrophysiological measures.

We could also identify the so-called belt fields (4) such as posterior–dorsal area (ref. 2 and Fig. 1*d*); this area is called posterior field in ref. 3. They appear as weak nontonotopic halos on the outer boundaries of the main fields (see Fig. 4). Finally, it also appears that the acoustically responsive cortex extends further ventrally than had been thought. The activation ventral and rostral to VAAF may reveal another auditory field (see Figs. 1*a* and 4; this field is marked by "?" in Fig. 4) or may constitute a ventral extensions of VAAF.

The optically defined frequencies were of sufficiently high quality and spatial resolution to conduct further quantitative description of the fields. The average cortical linear magnification factors in the central regions of the tonotopic fields along directions perpendicular to iso-frequency lines were: A1, 1.8 octave/mm; VAF, 2.2 octave/mm; VAAF, 2.9 octave/mm; and AAF, 2.3 octave/mm.

Comparison with maps obtained by standard electrophysiological mapping technique (Fig. 1*d*) reveals a high degree of correspondence. Our own dense electrophysiological mapping provided additional and direct confirmation of the optical maps (Fig. 2). Although there is a good agreement between optical and electrophysiological maps, one may note (Fig. 2*d*) a consistent deviation of the optical best frequencies (BFs) from the electrophysiological CFs in the lowest and highest octaves. The reason for this deviation is that stimulation for optical mapping was confined to 2–32 kHz, whereas stimulation for electrophysiology was centered at the CF of each multiunit site, which was in some cases near or beyond one of the extremes of the range of stimuli used for optical imaging. Thus, the receptive fields of units with CFs below ≈4 kHz and above ≈16 kHz were stimulated unevenly in the optical imaging, producing a shift of the optical BF toward the center of the stimulation range. This phenomenon will be referred to as the "stimulus boundary shift."

Another interesting observation was that the strength of optical response at a cortical site is not a monotonic function of the CF threshold at that site (Fig. 2 *e* and *f*). The optical response increases with decrease of the CF threshold until ≈30 dB SPL, 10 dB below intensity of stimulation for optical recording, and decreases for lower threshold values (Fig. 2*f*). This finding suggests that the signal measured by optical imaging has much broader tuning than the spiking activity. We will address this phenomenon in more detail in *Discussion*.

Comparison with Electrophysiological Suprathreshold Measures. The correlation analysis (Fig. 2*d*) compared data obtained at differ-

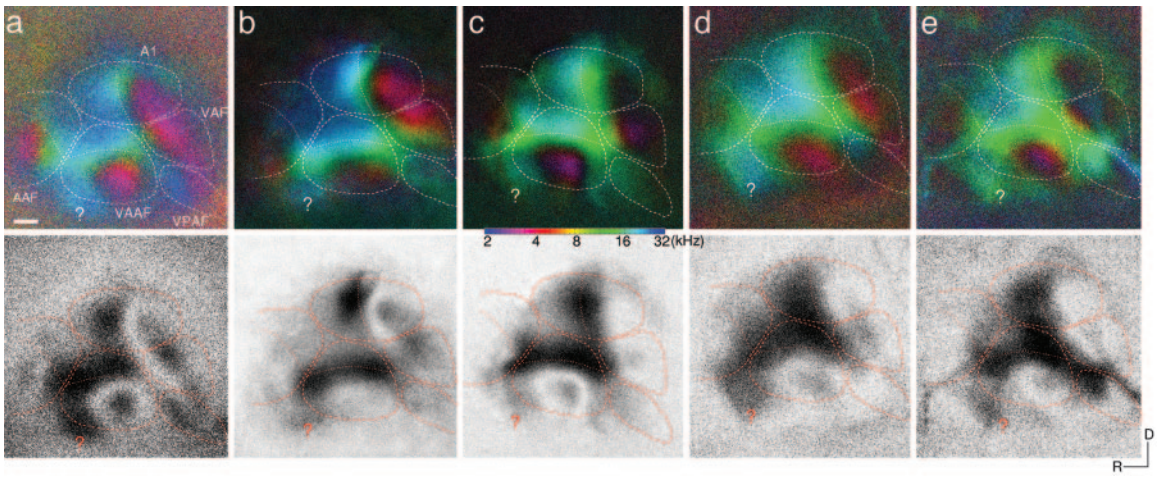

Fig. 4. Stability of multiple fields. Optical polar and magnitude maps, respectively, from five rats [ages 25, 50, 55 (male), 60, and 62 days] are shown. The contours were drawn on Fig. 1*c*, then transferred without any distortion to these figures, then translated and rotated until a match was achieved. The fields identified on Fig. 1*c* for P75 rat almost perfectly match the optically defined fields for all subjects. ''?'' labels possible additional auditory field. VPAF, ventral posterior auditory field.

ent experimental conditions, that is, the electrophysiological CFs, which are threshold measures, with optical BFs that were acquired at a constant sound intensity (40 dB SPL) and with a fixed range of stimulation (2–32 kHz). To further investigate the relationship between stimulus-evoked spiking and optical responses, we calculated four additional suprathreshold measures of the RFs at the intensity of stimulation used in optical imaging (see *Materials and Methods* for more details). The BFCMR and cosine curve fitting analyses were devised so that the electrophysiological data would better mimic the optical imaging condition with its fixed stimulation range. The Fourier measure corresponds to the procedure we followed to calculate optical BFs from the imaging data. Fig. 3 shows four tuning curves recorded in different representative auditory fields and compares suprathreshold measures with optical BFs.

These four suprathreshold measures and CF (threshold measure) were compared with optical BFs from maps acquired for upward and downward staircase stimuli and for the average map. Fig. 3*e* shows the RMS deviations of optical BFs from the electrophysiological spike measures as functions of optical threshold for the ascending staircase. The BFs from maps of relative tonotopy, such as ones shown in Fig. 5 *c* and *d*, are directly compared with unit data after shifting their phase by the hemodynamic delay. Only penetrations falling into regions of optical map where response strength was larger than a given threshold value were used for these comparisons. The BFCMR and Fourier RF measures consistently gave lowest RMS deviation, with the Fourier RF being exhibiting the highest correspondence (Fig. 3*e*). The best phase shifts for the Fourier frequencies were 81° and −86° for ascending and descending maps, respectively (calculated at doubled noise level or 30% threshold level), whereas the phase shift calculated via correlation of the ascending and descending optical maps was 83°. This high level of agreement of the phase shifts obtained by two independent methods clearly demonstrates the validity of the method of the stimulus reversal. Correlation scatter plot for optical imaging BFs from averaged map and electrophysiological Fourier frequencies is shown in Fig. 3*f* for one threshold level. Note that penetrations into weakly responsive optical region introduce large RMS deviations: all sites (CF threshold <40 dB SPL): $n = 110$; $R^2 = 0.93$, RMS deviation = 0.44 octave; sites above double optical noise level: $n = 91$, $R^2 = 0.96$, RMS deviation = 0.36 octave. The strong stimulus boundary shift evident in Fig. 2*d* was considerably reduced but not completely eliminated.

The significance of the strong correlation between the optical and electrophysiological maps was determined by Monte Carlo simulations. We associated the electrophysiological Fourier frequencies with the optical ones from randomly assigned penetrations into an optical map (Fig. 3*g*); random penetrations ($n = 110$) were allowed only inside the responsive area (white outline) but were disallowed over blood vessels, and the optical maps were then shifted for optimal correspondence, as was done for the real maps. The results of these simulations (10^6 trials) demonstrate a high confidence level for all RF frequency measures. The measured deviations for the real data are much less than were those for any of the simulations ($P < 0.00001$, Fig. 3*h*).

Discussion

Spiking Activity and Intrinsic Signals. It is accepted that the major source of optical intrinsic signals comes from metabolic activities and is attributed to changes in blood oxygenation level and blood volume (19, 28). The question of what is contributed by spiking activity to optical signals remains open. Here we demonstrated that optical BFs are similar to suprathreshold electrophysiological measures. However, there are at least two features that cannot be explained by spiking activity alone. First, although the strong stimulus boundary shift present in correlation of optical BFs and electrophysiological CFs (Fig. 2*d*) was considerably reduced when optical BFs were correlated with the Fourier frequencies (Fig. 3*f*), it was not completely eliminated. Second, optical maps have "valleys" of low amplitude response in the same regions where units have very robust, low-threshold responses (see Fig. 2 *e* and *f*; tuning curve shown in Fig. 3*a* comes from such a region). For example, the central regions of A1, VAF, and VAAF appear as islands surrounded by regions of weaker response. This phenomenon is clearly seen in Figs. 2*b*, 4, and 6*b*. Two distinct phenomena might lead to low optical responses in a cortical area: (*i*) the area is not responsive and (*ii*) the area responds similarly to all stimuli presented. The first reason can be dismissed, because microelectrode recordings in the valley regions show very robust responses. The second cannot be explained by spiking activity alone, because the bandwidth of the spike response from recorded units at the intensity of stimulation for optical imaging was only occasionally wider than ≈2 octaves, whereas the typical stimulus for imaging spanned 4

octaves. Furthermore, the correlation between the strength of the optical response and spiking bandwidth at the intensity of stimulation for optical imaging was not significant ($R^2 = -0.094$). These facts suggest that the optical signal in auditory cortex is evoked not only by spiking activity but also by other metabolic activities such as subthreshold membrane phenomena, which has been previously observed in visual (39) and somatosensory (40) cortices.

In summary, this paper describes a unique approach to optical imaging of intrinsic signals in auditory cortex. We show that this method is more efficient than traditional approaches at producing maps of tonotopy in the rat, and we use it to delineate at least five auditory areas with high spatial resolution. The sources of the improvement in quality and efficiency were discussed in details in our previous work (34). We provide an overall view of the structure of the auditory cortex in the rat, unambiguously delineating multiple auditory cortical areas and demonstrating their shapes, sizes, and tonotopic order. High-resolution maps obtained by the use of this optical imaging paradigm revealed fine details not only of the primary auditory cortex, which had been studied at moderate resolution with microelectrode recordings, but also for at least four additional areas of which little was known. Three of these additional areas also contain clear, fine-scale tonotopic organization. The multiple auditory cortical fields identified by optical imaging were highly similar among the large number of rats examined (e.g., Fig. 4), demonstrating not only that the mapping method is highly reproducible but that individual variability in normal animals is small.

The imaging method discussed here allows for a very rapid acquisition of rodent cortical maps. The spatial resolution of the technique is sufficiently reliable to resolve the internal structure of cortical areas as small as 300 μm. High-resolution maps of auditory cortex can be acquired in as fast as 5 min, a >100-fold reduction of the time consumed by the standard electrophysiological mapping technique, where it usually takes 10 h or more for dense mapping (>100 penetrations); thus, high-resolution maps allow detailed investigation of temporal features after quick noninvasive imaging sessions. Fourier optical imaging will be a very useful tool for rapid identification of cortical functional regions and quantitative measurements therein in future experiments concerning functional architecture and plasticity.

We thank Dr. Heather Read, Dr. Kazuo Imaizumi, and Andrew Tan for help during some experiments. The work was supported by the Sloan and Swartz Foundations and National Institutes of Health Grants EY 02874 and NS 16033.

1. Stiebler, I., Neulist, R., Fichtel, I. & Ehret, G. (1997) *J. Comp. Physiol. A* **181,** 559–571.
2. Horikawa, J., Ito, S., Hosokawa, Y., Homma, T. & Murata, K. (1988) *Proc. Jpn. Acad. Ser. B* **64,** 260–263.
3. Doron, N. N., Ledoux, J. E. & Semple, M. N. (2002) *J. Comp. Neurol.* **453,** 345–360.
4. Rutkowski, R. G., Miasnikov, A. A. & Weinberger, N. M. (2003) *Hear. Res.* **181,** 116–130.
5. Merzenich, M. M., Knight, P. L. & Roth, G. L. (1975) *J. Neurophysiol.* **28,** 231–249.
6. Knight, P. L. (1977) *Brain Res.* **130,** 447–467.
7. Reale, R. A. & Imig, T. J. (1980) *J. Comp. Neurol.* **192,** 265–291.
8. Phillips, D. P. & Orman, S. S. (1984) *J. Neurophysiol.* **51,** 147–163.
9. Schreiner, C. E. & Cynader, M. S. (1984) *J. Neurophysiol.* **51,** 1284–1305.
10. Imig, T. J., Ruggero, M. A., Kitzes, L. M., Javel, E. & Brugge, J. F. (1977) *J. Comp. Neurol.* **171,** 111–128.
11. Merzenich, M. M. & Brugge, J. F. (1973) *Brain Res.* **50,** 275–296.
12. Formisano, E., Kim, D. S., Di Salle, F., van de Moortele, P. F., Ugurbil, K. & Goebel, R. (2003) *Neuron* **40,** 859–869.
13. Riquimaroux, H., Gaioni, S. J. & Suga, N. (1992) *J. Neurophysiol.* **68,** 1613–1623.
14. Romanski, L. M., Tian, B., Fritz, J., Mishkin, M., Goldman-Rakic, P. S. & Rauschecker, J. P. (1999) *Nat. Neurosci.* **2,** 1131–1136.
15. Sally, S. L. & Kelly, J. B. (1988) *J. Neurophysiol.* **59,** 1627–1638.
16. Bonhoeffer, T. & Grinvald, A. (1996) in *Brain Mapping: The Methods,* eds. Toga, A. W. & Mazziotta, J. C. (Academic, New York), pp. 55–97.
17. Blasdel, G. G. & Salama, G. (1986) *Nature* **321,** 579–585.
18. Grinvald, A., Lieke, E., Frostig, R. D., Gilbert, C. D. & Wiesel, T. N. (1986) *Nature* **324,** 361–364.
19. Bonhoeffer, T. & Grinvald, A. (1991) *Nature* **353,** 429–431.
20. Masino, S. A., Kwon, M. C., Dory, Y. & Frostig, R. D. (1993) *Proc. Natl. Acad. Sci. USA* **90,** 9998–10002.
21. Narayan, S. M., Santori, E. M. & Toga, A. W. (1994) *Cereb. Cortex* **4,** 195–204.
22. Godde, B., Hilger, T., von Seelen, W., Berkefeld, T. & Dinse, H. R. (1995) *NeuroReport* **7,** 24–28.
23. Chen, L. M., Friedman, R. M. & Roe, A. W. (2003) *Science* **302,** 881–885.
24. Rubin, B. D. & Katz, L. C. (1999) *Neuron* **23,** 499–511.
25. Uchida, N., Takahashi, Y. K., Tanifuji, M. & Mori, K. (2000) *Nat. Neurosci.* **3,** 1035–1043.
26. Meister, M. & Bonhoeffer, T. (2001) *J. Neurosci.* **21,** 1351–1360.
27. Belluscio, L. & Katz, L. C. (2001) *J. Neurosci.* **21,** 2113–2122.
28. Frostig, R. D., Lieke, E. E., Tso, D. Y. & Grinvald, A. (1990) *Proc. Natl. Acad. Sci. USA* **87,** 6082–6086.
29. Mayhew, J. E. W., Askew, S., Zheng, Y., Porrill, J., Westby, G. W. M., Redgrave, P., Rector, D. M. & Harper, R. M. (1996) *NeuroImage* **4,** 183–193.
30. Bakin, J. S., Kwon, M. C., Masino, S. A., Weinberger, N. M & Frostig, R. D. (1996) *Cereb. Cortex* **6,** 120–130.
31. Schulze, H., Hess, A., Ohl, F. W. & Scheich, H. (2002) *Eur. J. Neurosci.* **15,** 1077–1084.
32. Versnel, H., Mossop, J. E., Mrsic-Flogel, T. D., Ahmed, B. & Moore, D. R. (2002) *J. Neurophysiol.* **88,** 1545–1558.
33. Tsytsarev, V. & Tanaka, S. (2002) *NeuroReport* **13,** 1661–1666.
34. Kalatsky, V. A. & Stryker, M. P. (2003) *Neuron* **38,** 529–545.
35. Nelken, I., Bizley, J. K., Nodal, F. R., Ahmed, B., Schnupp, J. W. H. & King. J. A. (2004) *J. Neurophysiol.* **92,** 2574–2599.
36. Zhang, L. I., Bao, S. & Merzenich, M. M. (2001) *Nat. Neurosci.* **4,** 1123–1130.
37. Zhang, L. I., Bao, S. & Merzenich, M. M. (2002) *Proc. Natl. Acad. Sci. USA* **99,** 2309–2314.
38. Bao, S., Chang, E.F., Davis, J.D., Gobeske, K.T. & Merzenich, M.M. (2003) *J. Neurosci.* **23,** 10765–10775.
39. Toth, L. J., Rao, S.C., Kim, D.S., Somers, D. & Sur, M. (1996) *Proc. Natl. Acad. Sci. USA* **93,** 9869–9874.
40. Takashima, I., Kajiwara, R. & Iijima, T. (2001) *NeuroReport* **12,** 2889–2894.